Biomaterials 182 (2018) 269–278

Contents lists available at ScienceDirect

Biomaterials

journal homepage: www.elsevier.com/locate/biomaterials

Tumor-triggered transformation of chimeric peptide for dual-stage-amplified magnetic resonance imaging and precise photodynamic therapy

Jin Zhang[a], Yong-Li Mu[b], Zhao-Yu Ma[b], Kai Han[b,**], He-You Han[a,*]

[a] State Key Laboratory of Agricultural Microbiology, College of Life Science and Technology, College of Science, Huazhong Agricultural University, Wuhan, 430070, Hubei, PR China

[b] State Key Laboratory of Agricultural Microbiology, College of Science, Huazhong Agricultural University, Wuhan, 430070, Hubei, PR China

ARTICLE INFO

Keywords:
Chimeric peptide
MMP-2
Transformation
MRI enhancement
Photodynamic therapy

ABSTRACT

Despite the great success in clinical magnetic resonance imaging (MRI), Gd^{3+}-based contrast agents still suffer from low proton relaxation efficiency, rapid metabolic clearance as well as poor sensitivity. In this work, we designed a matrix metalloproteinase-2 (MMP-2) responsive chimeric peptide for dual-stage-amplified MRI and precise photodynamic therapy. Both *in vitro* and *in vivo* studies indicated that this chimeric peptide could self-assembly into spherical nanoparticles at physiological condition with r_1 value of 28.17 $mM^{-1}s^{-1}$. Meanwhile, the spherical shape endowed chimeric peptide with efficient tumor accumulation *via* enhanced penetration and retention (EPR) effect. Importantly, the overexpressed MMP-2 in tumor region could specifically hydrolyze chimeric peptide, leading to sphere-to-fiber transformation. This transformation enhanced both the tumor accumulation and the relaxivity of contrast agent. Consequently, the r_1 value was remarkably elevated to 51.52 $mM^{-1}s^{-1}$, which guided precise photodynamic therapy. This tumor microenvironment-triggered transformable strategy should show great potential for tumor-targeted imaging and phototherapy.

1. Introduction

With the rapid progress of nanomedicine, multifunctional nanoparticles have shown extraordinary potential as theranostic agents in bioimaging, phototherapy, drug delivery [1–4]. Among them, a variety of biomacromolecules, organic nanoparticles, inorganic nanoparticle and nanogels have been developed to solve the intrinsic drawbacks associated with clinical small molecular contrast agents, such as low proton relaxation efficiency, relatively low sensitivity and rapidly clearance from body [5–10]. Unfortunately, these nanoparticles realize tumor specific imaging strongly depending on alternate the biodistribution of contrast agents through the active targeting and passive targeting. Other crucial parameters in MRI including relaxivity were ignored to some extent [11–13]. In order to improve the imaging, some "smart" or "activatable" MR probes in response to unique tumor environment (such as lower pH, H_2O_2, high reduction potential, overexpressed enzymes) has also been exploited to amplify MRI signal by modulating their relaxivity [14–20]. However, the use of either paramagnetic Mn^{2+} or Gd^{3+} chelates also was limited owing to their low MR properties (e.g., low relaxivity). Therefore, the development of a multifunctional nanosystem which can both possess higher relaxivity and satisfactory accumulation in tumor would optimize the imaging performance.

Recently, some pioneering works have confirmed that the fiber-shaped contrast agents exhibit higher relaxivity value, when compared with the spherical counterparts. Meanwhile, it is also recognized that the long fiber-shaped nanoparticles have prolonged tumor retention in tumor [21–23]. All these issues indicate that fiberous nanostructure contrast agents will be more suitable for MRI [24–26]. Unfortunately, current studies mainly highlight systemically comparing the MRI signal change between spherical and fibril nanoparticles *in vitro*. The *in vivo* application of these fiber-shaped contrast agents are still scarcely reported, partly because of the fibrillar nanoparticles could not discern between tumor tissue and healthy tissue. On the other hand, fiber-shaped nanoparticles always lower hydrophile-lipophilic-balance, which will result in the potential instability *in vivo*. More importantly, although fiber shape endows the nanoparticles with long blood retention time, the great aspect ratio restricts them to cross the blood vessel wall, resulting in low tumor accumulation efficacy.

Keep all these issues in mind, we reported a tumor-triggered transformable chimeric peptide PpiX-PEG_8-SSSPLGLAK (DOTA)-PEG_6-F_4 (denoted as Ppdf-Gd) for MRI amplification guided photodynamic

* Corresponding author.
** Corresponding author.
E-mail addresses: hank@mail.hzau.edu.cn (K. Han), hyhan@mail.hzau.edu.cn (H.-Y. Han).

https://doi.org/10.1016/j.biomaterials.2018.08.026
Received 26 March 2018; Received in revised form 8 August 2018; Accepted 8 August 2018
Available online 11 August 2018
0142-9612/

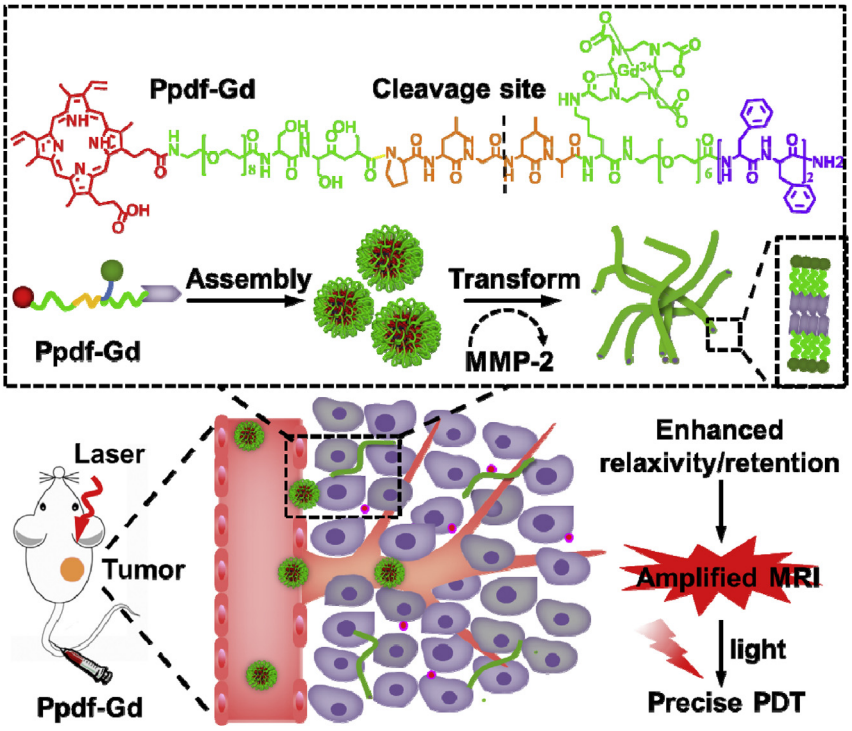

Scheme 1. Schematic illustration of MMP-2-triggered transformation of Ppdf-Gd from spherical nanoparticles to nanofibers and the principle of dual-stage-amplified MRI and PDT. Ppdf-Gd can self-assembly to spherical nanoparticles in physiological conditions. When reaching tumor tissue by the EPR effect, the nanoparticles underwent sphere-to-fibers transformation under MMP-2. This transformation can enhance relaxivity and retention of contrast agent in tumor region, which realized amplified MRI and precise PDT.

therapy. As shown in Scheme 1, this amphiphilic Ppdf-Gd can self-assembly to spherical nanoparticles in neutral conditions. When the nanoparticles arrived at tumor site, the overexpressed MMP-2 would hydrolyze the Pro-Leu-Gly-Leu-Ala (PLGLA) peptide sequence, resulting in generation of LAKDOTA(Gd)-PEG_6-F_4 fragment as well as PEGylated photosensitizer protoporphyrin IX (PpiX). The π-π stacking interaction among Phe amino acids and hydrogen bond within peptide chain would drive LAKDOTA(Gd)-PEG_6-F_4 to form long fibers, which could improve the accumulation and retention of DOTA(Gd) in tumor. Importantly, the sphere-to-fiber switch led to higher relaxation rate of DOTA(Gd). These two issues would amplify the MRI signal in tumor, which guided photodynamic therapy precisely.

2. Materials and methods

2.1. Reagents and materials

Rink Amide resin, N-fluorenyl-9-methoxycarbonyl (Fmoc)-protected L-amino acids, diisopropylethylamine (DIEA), o-benzotriazole-N,N,N′,N'-tetramethyluroniumhexafluorophosphate (HBTU) and piperidine were purchased from GL Biochem Ltd. (Shanghai, China). Thioflavin T and tri-tert-butyl 1,4,7,10-tetraazacyclododecane-1,4,7,10-tetraacetate (DOTA) was purchased from Sigma-Aldrich. Dulbecco's modified Eagle's medium (DMEM), trypsin, fetal bovine serum (FBS), MTT, penicillinstreptomycin were purchased from GIBCO Invitrogen Corp. Triisopropylsilane (TIS), Gadolinium (III) chloride hexahydrate ($GdCl_3.6H_2O$), and trifluoroacetic acid (TFA) were obtained from Shanghai Reagent Chemical Co. (China). All other reagents and solvents were used directly.

2.2. Synthesis of Ppdf-Gd and Pdf-Gd

Ppdf was manually synthesized *via* conventional solid phase peptide synthesis procedure (SPPS) method on Rink Amide resin (0.596 mmoL/g). After the resin was swollen in DMF for over 1 h in nitrogen atmosphere, Fmoc group deprotection was performed used 20% piperidine in DMF at room temperature for 20 min. HBTU/DIPEA was used as coupling agents to sequentially couple amino acids to the N-terminus of peptide on resin. DOTA was introduced to peptide chain by coupling to ε-NH_2 of Lys using FMOC-Lys (Mtt)—OH as a linker. The Ppdf was cleaved from the resin by a cleavage solution (TFA: TIS: H_2O = 95: 2.5: 2.5) for 1.5 h. Then the crude product was prepared by precipitated the mixed solution in cold anhydrous diethyl ether and drying under vacuum overnight. The crude was dissolved in distilled water and freeze-drying to obtain Ppdf. The purity of Ppdf was analyzed by High-performance liquid chromatography (HPLC) using SP-120-5-C4-BIO column (4.6 * 250 mm) with acetonitrile (0.1% of TFA) and water (0.1% of TFA) as the eluent. The molecular weight was verified by electrospray ionization mass spectrometry (ESI-MS).

To prepare Ppdf-Gd, $GdCl_3.6H_2O$ was added to Ppdf solution (molar ratio = 1: 1.1) at pH 6.5 and then stirred overnight at room temperature [21]. The resulting compound was purified by HPLC over Boston Crest ODS column (4.6 * 250 mm) with acetonitrile (0.1% of TFA) and water (0.1% of TFA) as the eluent. The gradient was: 0–5 min 30% CH_3CN and 70% H_2O; 5–20 min 70% CH_3CN and 30% H_2O; 20–30 min 100% CH_3CN. The molecular mass was confirmed by ESI-MS. As control, the Pdf-Gd was obtained by the similar method.

2.3. UV–vis spectrum and reactive oxygen species (ROS) detection

UV–vis absorption spectrum of Ppdf-Gd (50 mg/L) was determined at neutral pH. The generation of ROS was measured using DCFH-DA as the sensor. Ppdf-Gd (20 μL, 1 g/L) and DCFH-DA (250 μL, 20 mg/L) were mixed with 730 μL water in a quartz cuvette. The cuvette was light irradiated by 630 nm laser at preset time. The fluorescence spectrum with a range from 500 to 550 nm was recorded with an excitation wavelength of 488 nm. Free PpiX in 0.02% DMSO was used as a negative control. The ROS generation ability was calculated as the formula: F_t/F_0. F_0 was initial fluorescence of samples without irradiation. F_t represented the fluorescence of samples with a certain time irradiation.

2.4. Circular dichroism (CD) measurement

CD spectra were measured using a J-1500 spectropolarimeter (Jasco, Japan). MMP-2 (20 μL, 100 μg/L) was added to Ppdf-Gd solution

(0.25 g/L) with a total volume of 0.5 mL. The CD spectrums were recorded immediately from 240 to 190 nm at 0, 1, and 3 h. The CD spectrums were repeated three times and averaged. The Pdf-Gd served as a control.

2.5. Transmission electron microscope (TEM) and hydrodynamic size measurement

The hydrodynamic size was measured by Nano-ZS ZEN3600 (Malvern Instruments). Ppdf-Gd (25 mg/L) was incubated with MMP-2 (100 μg/L) in PBS buffer. After incubated with MMP-2 for 0 and 6 h, hydrodynamic size was tested at 25 °C. The morphology of Ppdf-Gd was examined by TEM (JEM-2100 microscope). When Ppdf-Gd was incubated with MMP-2 for 0 and 6 h, the TEM samples were prepared by dropping the solution onto carbon-coated copper grids and evaporated under vacuum condition.

2.6. Critical aggregate concentration (CAC) determination

The CAC values were measured by fluorescence spectroscopy using pyrene as a probe. Pyrene (6×10^{-6} M) was dissolved with 100 μL acetone and then open the vial cap overnight until the acetone was evaporated completely. Thereafter, 1 mL Ppdf-Gd solution with various concentrations (0–0.1 mg/mL) was added to vial. After 20 min sonication, excitation spectra from 300 to 360 nm were recorded (EM: 390 nm). The intensity ratio of the third and first vibronic bands (I_3/I_1) was plotted against the logarithm of Ppdf-Gd concentrations. The CAC value was obtained based on the abscissa value of the crossover point. To test the MMP-2 responsiveness, Ppdf-Gd was incubated with MMP-2 (40 μL, 100 μg/L) for 6 h. Then the CAC was determined in a similar way.

2.7. Cytotoxicity assay

The cytotoxicity of Ppdf-Gd against SCC-7 cells was determined by MTT assay. SCC-7 cells were seeded on 96-well plates at a density of 6000 cells/well. After 24 h incubation, the medium was replaced with various concentrations of Ppdf-Gd. After 4 h incubation, the culture medium was replaced with 200 μL of fresh medium. Subsequently, cells received 50 s light irradiation (630 nm, 10 mW/cm^2) and were further incubated for 48 h. 20 μL MTT (5 mg/mL) was added per well. Four hours later, the supernatant was removed and 150 μL DMSO was added to dissolve the formazane. The optical density (OD) at 490 nm was determined *via* a microplate reader (Bio-Rad, Model 550, USA). The relative cell viability was calculated based on the formula: cell viability (%) = $OD_{(sample)}/OD_{(control)} \times 100\%$. $OD_{(sample)}$ was the OD value in the presence of sample and $OD_{(control)}$ was the optical density in the absence of sample.

2.8. Relaxivity measurement

A series of DOTA-Gd, Ppdf-Gd, and Ppdf-Gd solution were prepared at different Gd^{3+} concentration of 0, 0.0025, 0.005, 0.01, and 0.02. The T1 time was measured using a Bruker 4.7 T Pharmascan MRI system. Relaxivity was calculated as the slope of linear fit of longitudinal relaxation rate (1/T1) versus the Gd^{3+} concentration. The groups of Ppdf-Gd and Pdf-Gd with MMP-2 were obtained by pretreated with additional MMP-2 (40 μL, 100 ng/mL) for 6 h. True Gd^{3+} concentration was determined by ICP-MS.

2.9. In vivo MR image

In vivo MR imaging was conducted on a Bruker 7 T Pharmascan MRI system. The SCC-7 tumor-bearing nude mice were anesthetized using 5% chloral hydrate (250 μL) *via* intraperitoneal injection. DOTA-Gd, Ppdf-Gd and Pdf-Gd were infected *via* tail vein at a dose of 0.05 mmoL/kg Gd^{3+} per mice. Then, the MR images of mouse were recorded at preset time. Quantitative analysis was conducted using Image J. Signal increment ratio in tumor region had been calculated as $intensity_{post\text{-}injection}/intensity_{pre\text{-}injection}$. $Intensity_{post\text{-}injection}$ was the initial gray scale. The following parameters: TR/TE = 500/11 ms; matrix: 256 × 256; number of excitations: 2.0; slice thickness = 1 mm; slice gap = 0 mm; FOV: 3.0 cm; and coil: RAT HEAD/MOUSE BODY VOLUME.

2.10. Optical imaging, tissue distributions and pharmacokinetics in vivo

Animal experiments were conducted in compliance with the criteria of The National Regulation of China. SCC-7 tumor-bearing female nude mice were used as animal model. Ppdf-Gd (200 μL, 5 mg/kg PpiX per mouse) was injected into mouse *via* tail vein. The optical imaging study was performed by small animal imaging system at the preset times. 24 h later, mice were sacrificed and the heart, liver, spleen, lung, kidney, and tumor were exfoliated and imaged for tissue distribution study.

For the pharmacokinetic study, Ppdf-Gd (5 mg/kg PpiX per mouse) was intravenously injected into SCC-7 tumor-bearing nude mice. At a preset time, 15 μL blood samples were collected *via* the tail vein. The blood samples were diluted to 700 μL and then repeated freeze-thawed to disrupt the cells. After 5 min sonication, the samples were centrifuged (5 min, 3000 r/min) and the supernate was measured using fluorescence spectrum to obtain the amount of PpiX. For biodistribution analysis of Gd^{3+}, Ppdf-Gd and Pdf-Gd were injected intravenously at the dose of 0.05 mmoL/kg Gd^{3+} per mouse. At 3 and 24 h postinjection, the tumors and main organs (heart, lung, liver, spleen, and kidney) were collected, weighed, and digested with the HNO_3/H_2O_2 solution (HNO_3/H_2O_2 volume ratio = 4:1). The Gd contents in organs and tumors were measured using ICP-MS. The results were converted to the percentage of injected dose per gram of tissue (%ID g^{-1}).

2.11. In vivo antitumor therapy

5×10^6 of SCC-7 tumor cells (100 μL) was injected subcutaneously into the nude mice. When the volume of SCC-7 tumor xenograft growth was around 100 mm^3, mice were randomly divided into 4 groups. Ppdf-Gd was intravenously injected into mice at the dose of 4 mg/kg PpiX concentration every day. For PpiX group, PpiX in DMSO (50 μL) was injected into mice *via* intraperitoneal injection. 6 h postinjection, mice received 10 min light irradiation (633 nm, 0.2 W/cm^2). The tumor volume and body weight were measured per day. The tumor volume was calculated as following: $a \times b^2/2$, a and b referred to the length and width of tumor, respectively. At the ending of treatment, the tumors in various groups were exfoliated, weighted and photographed for further evaluate antitumor effective.

2.12. Systemic toxicity in vivo

For serum analysis, the mice blood was extracted from different mice groups *via* at the ending of treatment. The blood samples were solidified and centrifuged at 3000 rpm for 5 min. Then, serum samples were collected and detected at Union Hospital (Wuhan, China). Data were mean of three replicates. For histological observation, mice were sacrificed at the end of treatment. The organs and tumor were exfoliated and fixed by 4% formalin. Then they were embedded in paraffin for H&E staining.

2.13. Statistical analysis

The statistical analysis was determined by Student's t-test. The differences were considered to be statistically significant for p value < 0.05.

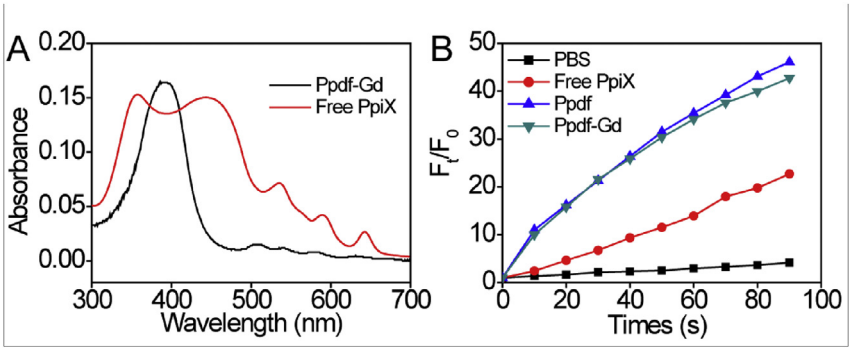

Fig. 1. (A) UV–vis spectrum of Ppdf-Gd and PpiX. (B) ROS generation of Ppdf and Ppdf-Gd with different light irradiation times. DCFH-DA was used as the sensor. PBS and PpiX in 0.05% DMSO were used as controls.

3. Results and discussion

3.1. Synthesis and characterization of Ppdf-Gd

Ppdf was synthesized *via* the solid-phase peptide synthesis (SPPS) method (See Fig. S1 for preparation details). HPLC (Fig. S2) indicated that the purity of Ppdf was above 90%. The molecular weight of Ppdf was confirmed by ESI-MS (Fig. S3). To incorporate Gd^{3+} into Ppdf, $GdCl_3.6H_2O$ was mixed with chimeric peptide with a mole ratio of 1:1.1 at pH 6.5 and reacted for 24 h. The resulting compound was purified by HPLC and the compound was identified by ESI-MS (Fig. S4 and S5). The UV–vis spectrum (Fig. 1A) showed that the soret band of Ppdf-Gd was a single-peak around 400 nm, indicating little π-π stacking-induced aggregation occurred among PpiX molecules. On the contrary, the free PpiX had broadened dual-peaks at 352 nm and 450 nm [27]. The reduction of π-π stacking among PpiX molecules in Ppdf-Gd also facilitated the generation of ROS. 2′, 7′-dichlorofluorescin diacetate (DCFH-DA) was used as a ROS probe to evaluate the generation efficacy of ROS. As shown in Fig. 1B, the fluorescence in Ppdf-Gd group increased faster than that in both PBS group and PpiX group under light irradiation, suggesting that Ppdf-Gd nanoparticles could transfer the light energy to surrounding dissolved oxygen (O_2) more efficiently. Meanwhile, a curve similar to Ppdf-Gd was found in Ppdf suggested that the introduction of Gd^{3+} did not affect the ROS generation.

3.2. MMP-2 triggered transformation of Ppdf-Gd

To observe the self-assembly behavior of Ppdf-Gd, dynamic light scattering (DLS) and TEM image was conducted. It was found that the hydrodynamic size of amphiphilic Ppdf-Gd around 120 nm at pH 7.4 (Fig. 2A1). TEM results further revealed that Ppdf-Gd could form well-dispersed spherical nanoparticles (Fig. 2B1). Note that nanoparticles in the sub-200 nm range always had great potential in preferentially accumulating in tumor tissue [28]. There was discrepancy in the hydrodynamic size and TEM size due to the shrinkage of self-assembly during the preparation of TEM samples. TEM sample was air-dried and the observation was under high vacuum, resulting in evaporation of water and dramatically collapse of complexes.

Considering that PLGLA peptide sequence could be specifically cleaved by enzyme MMP-2 [29,30], it would lead to generation of LAKDOTA(Gd)-PEG_6-F_4 (M2) sequence (Fig. S7A). The tetra-phenylalanine as a self-assembly initiator might change the self-assembly behavior of Ppdf-Gd [31]. In order to confirm it, the self-assembly behavior of Ppdf-Gd in the presence of MMP-2 was investigated. DLS results showed that a new peak over 1 μm appeared (Fig. 2A2). These results indicated that some large size self-assembly emerged in the presence of MMP-2. TEM result revealed that many fibers with several microns in length appeared (Fig. 2B2). The amplified image further revealed that the diameter of these fibers was around 13.63 nm (Fig. 2C). For comparison, the self-assembly of MMP-2 insensitive peptide PpiX-PEG_8-SSSLPALG-K (DOTA)-PEG_6-F_4 (denoted as Pdf-Gd, the structural formula was showed in Fig. S1) was also investigated. As expected, Pdf-Gd exhibited similar size to Ppdf-Gd as depicted in Fig. 2A3 and B3. In contrast, both the hydrodynamic size (Fig. 2A3 and A4) and morphology (Fig. 2B3 and B4) of Pdf-Gd had little change after addition of MMP-2, suggesting that MMP-2 could effective hydrolyze Ppdf-Gd and mediate the sphere-to-fiber transformation. The dynamic sphere-to-fiber transformation process was also monitored by TEM as a function of time in Fig. 2D. After incubated with MMP-2 for 1 h, some irregular nanoparticles appeared. When the incubation time to 2 h, these irregular nanoparticles gradually changed to rod-like nanoparticles. Interestingly, when Ppdf-Gd was incubated with MMP-2 only for 3 h, many distinct fibers with great aspect ratio formed, and some fibers intertwined together to generate some particles with several micrometer. Clearly, Ppdf-Gd had high MMP-2 sensitivity and the sphere-to-fiber transformation can occur within 3 h. Noted that the morphology observed in Fig. 2C and D was different, since the lower concentration of Ppdf-Gd was chosen in Fig. 2C.

Besides, the structure of another fragment (PpiX-PEG_8-SSSPLG, M1) was also investigated due to it play an important role in PDT. For observing his structure separately, we extra synthesized M1. The TEM result (Fig. S7B) revealed that it could self-assembly into spherical nanoparticles with a well-dispersibility due to the abundant hydrophilic fragments such as PEG_8 and serine. Subsequently, we also tested the fluorescence change of Ppdf-Gd with MMP-2 in mixture. Interestingly, a gradually increased fluorescence was found over time (Fig. S7C) suggested that less aggregation of PpiX molecules appeared after addition of MMP-2 according to aggregation-caused quenching (ACQ) effect. A more efficient ROS generation further confirmed that the enhanced hydrophilicity of PpiX after addition of MMP-2 (Fig. S7D), while no change occurred in Pdf-Gd (Fig. S7E). The enhanced ROS genration could lead to better therapeutic efficiency in PDT.

3.3. Transformation mechanism study of Ppdf-Gd

To get insight of the transformation mechanism, Ppdf-Gd was incubated with MMP-2 and the change of secondary structure was recorded using CD spectrum at preset time. Similar to previous reports, Ppdf-Gd exhibited two positive peaks around 205 and 218 nm (Fig. 3A) due to stacking interactions among aromatic units [32]. A single minimum at 228 nm indicated the existence of *β*-sheet structure. Interestingly, when Ppdf-Gd incubated with MMP-2, the peak intensity at 205 nm and 218 nm gradually decreased while the peak at 228 nm didn't change. These results indicated that *β*-sheet structure became the dominant secondary structure with the hydrolysis of PLGLA sequence [25,33,34]. In sharp contrast, negligible change was observed in the CD spectrum of Pdf-Gd (Fig. 3B), which substantially demonstrated that

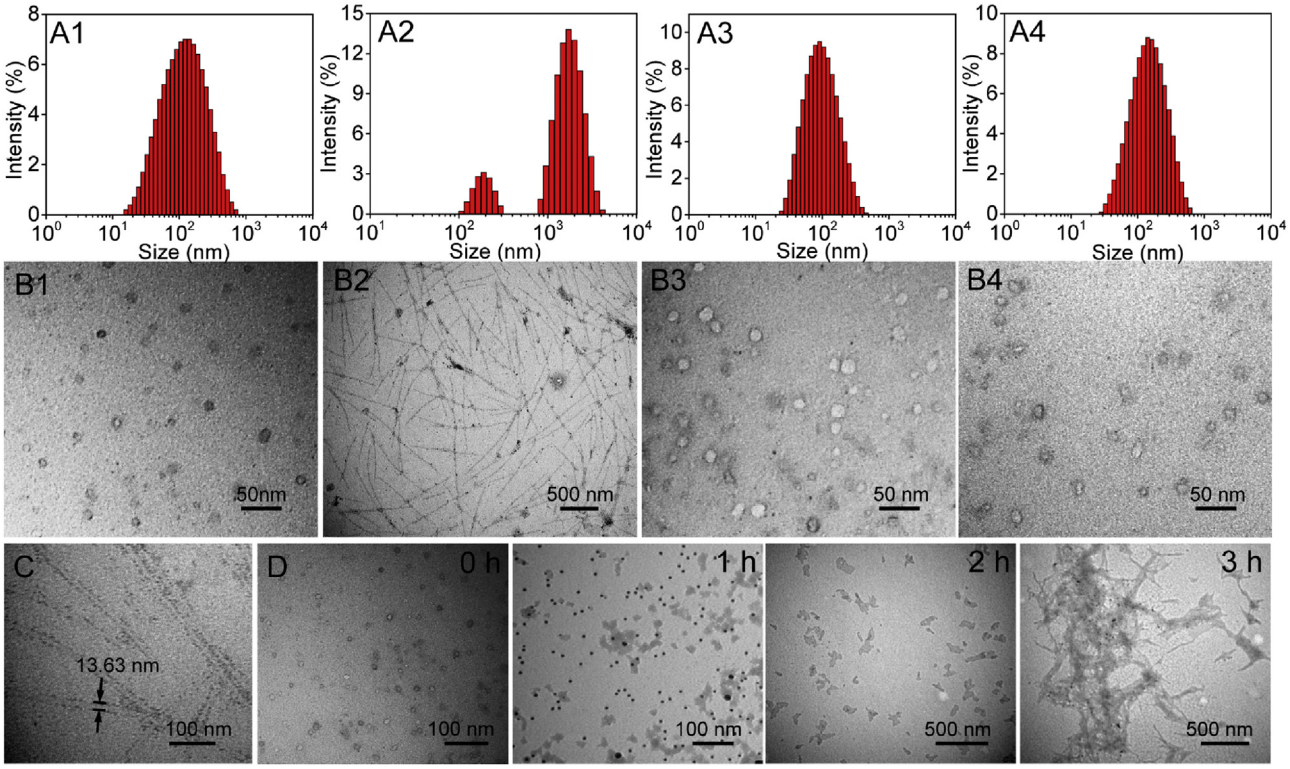

Fig. 2. Hydrodynamic size and TEM images of Ppdf-Gd solution (A1, B1) in the presence or (A2, B2) the absence of MMP-2. Hydrodynamic size and TEM image of Pdf-Gd solution (A3, B3) in the absence or (A4, B4) the presence of MMP-2. (C) Amplified TEM image of Ppdf-Gd. (D) TEM images for morphology changes. The TEM images of 0, 1, 2, and 3 h were recorded after Ppdf-Gd was incubated with MMP-2 (100 ng/mL).

MMP-2 play a key role in the change of the secondary structure. In addition, Thioflavin T (ThT) spectroscopic assay was also conducted to future confirmed the variation of secondary structure. ThT is a classical probe which can detect amyloid formation due to its emission peak at 482 nm would increase upon binding to β-sheet structures. As shown in Fig. 3C, the fluorescence intensity of ThT at 482 nm was relatively stable, when ThT or Pdf-Gd was incubated with MMP-2. However, fluorescence intensity of ThT in Ppdf-Gd group presented a remarkable increment in the presence of MMP-2, suggesting that more β-sheet transition appeared which was also in agreement with the CD results.

In order to further understand the principle, CAC of Ppdf-Gd was determined with a fluorescence-based method using pyrene as probe. The CAC value of Ppdf-Gd was calculated to be 15.8 mg/L (Fig. 3D). However, after the introduction of MMP-2, the CAC value of Ppdf-Gd decreased to 6.3 mg/L (Fig. 3E). The lower CAC value indicated that the hydrolysis of PLGLA sequence by MMP-2 enhanced the hydrophobicity and mediated the β-sheet transition of chimeric peptide, which subsequently drove sphere-to-fiber transition [35].

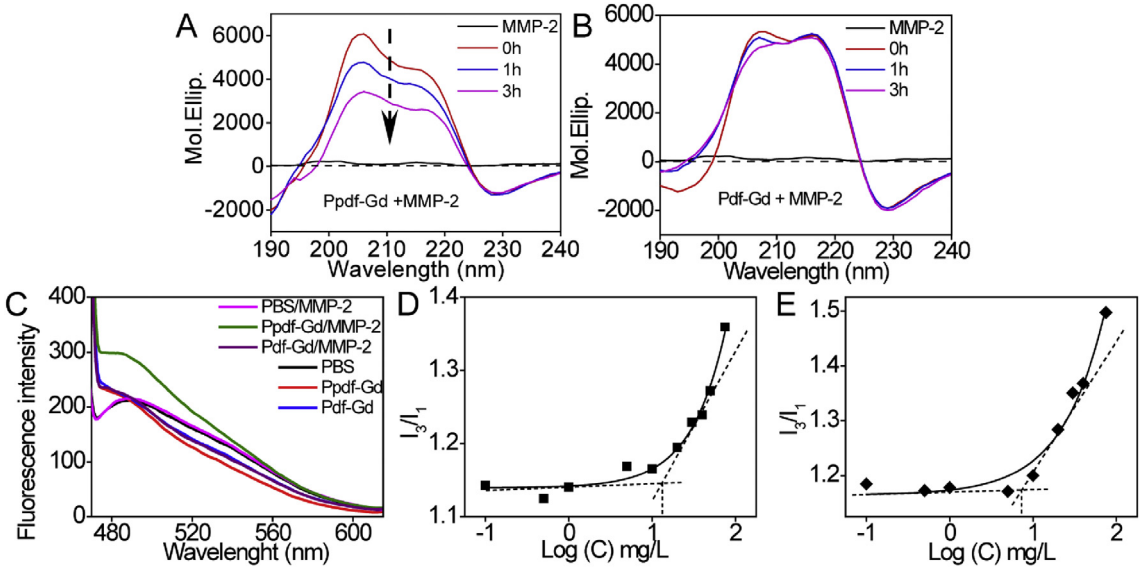

Fig. 3. CD spectrum of (A) Ppdf-Gd and (B) Pdf-Gd after incubated with MMP-2 for 0, 1 and 3 h. (C) Fluorescence spectrum of ThT dye (250 μM) with Ppdf-Gd or Pdf-Gd after 0 and 12 h incubation, respectively. CAC values measurement of Ppdf-Gd before (D) and after (E) incubated with MMP-2. Pyrene was used as a sensor.

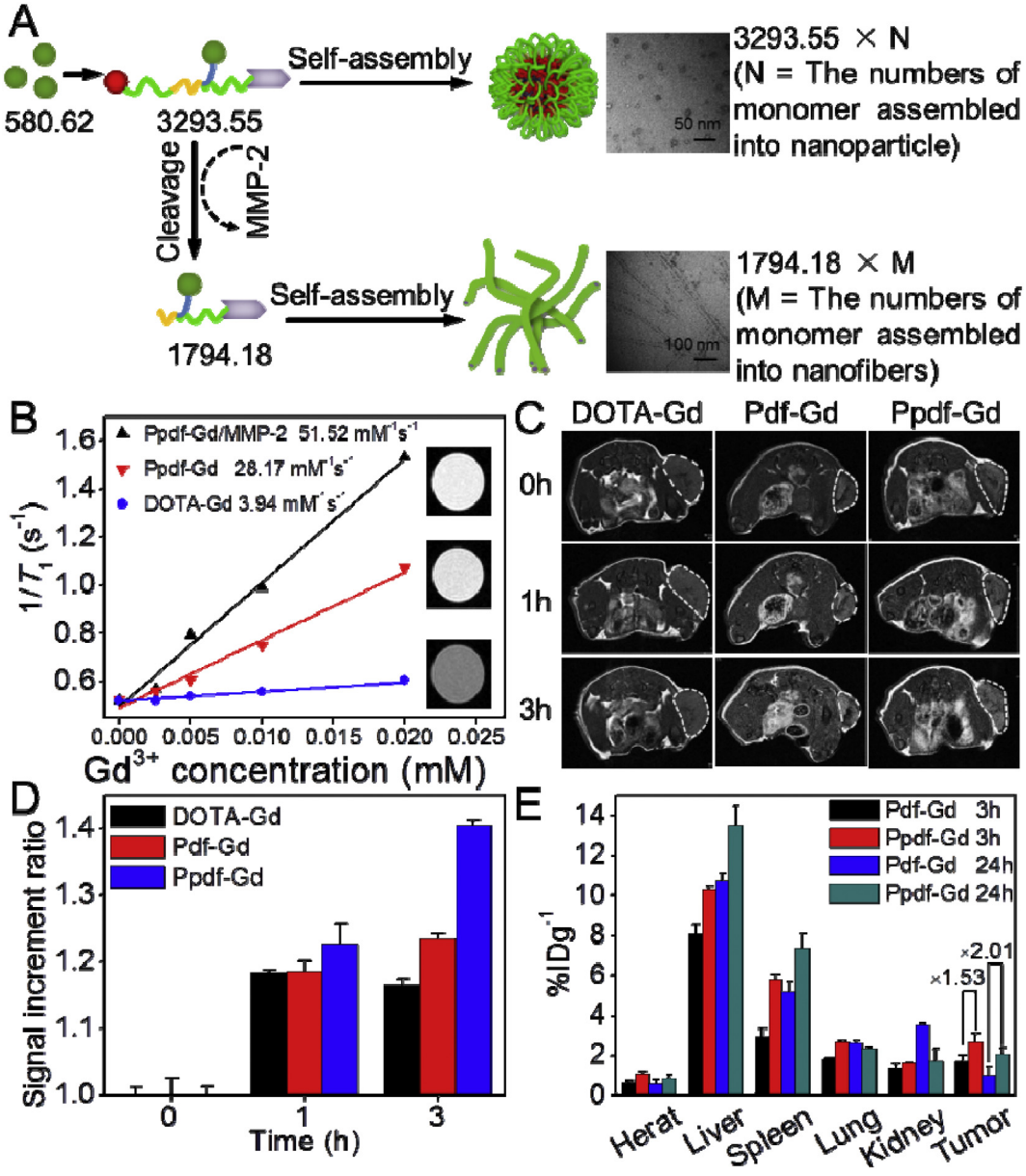

Fig. 4. (A) Schematic illustration of the molecular weight calculation for DOTA-Gd, spherical nanoparticle and nanofiber. (B) Longitudinal relaxation rates measurement of Ppdf-Gd, DOTA-Gd and Ppdf-Gd with enzyme MMP-2. The insets represented the T1 weighted MR images of various groups at same Gd^{3+} concentration. (C) T1-weighted MRI images of mice at 0, 1, and 3 h after intravenous (*i.v.*) injection (Gd^{3+} dose: 0.05 mmoL/kg). (D) Signal increment ratio in tumor area, the value was set as $signal_{pre\text{-}injection}/signal_{post\text{-}injection}$. The signal intensity was measured *via* Image J software. (E) Biodistribution of Gd^{3+} content in various organs and tumor after intravenous injection of Ppdf-Gd, the Gd^{3+} content were detected by ICP-MS.

3.4. Sphere-to-fiber transformation mediated amplified MRI

According to the Solomon–Bloembergen–Morgan (SBM) equations, there are many factors that can determine the relaxation rate of Gd^{3+} chelate contrast agents, such as concentration r, the number of inner-sphere water molecules (q), the water exchange rate (k_{ex}), the tumbling rate ($1/t_R$), scalar (SC) and a dipole-dipole (DD). However, when the field strengths higher than 0.25 T (> 10 MHz), the relaxivity of nanoparticles is dominated by the tumbling rate in most small contrast agents. Importantly, larger molecular weight objects will have a lower tumbling rate, follow by led to a higher relaxivity [36–38]. Encouragingly by Ppdf-Gd could undergo MMP-2-triggered sphere-to-fiber transformation, we investigated whether the sphere-to-fiber transformation would affect the relaxivity. Above all, we simply evaluated the molecular weight of DOTA-Gd, nanoparticle and nanofiber. As shown in Fig. 4A, the molecular weight of Ppdf-Gd monomer before and after enzyme addition of MMP-2 is 3293.55 and 1794.18, respectively. Because of these amphiphilic monomers would self-assembly to nanoparticles or nanofibers in solution. The DOTA attached to the nanoparticles would tumble within the nanoparticles or fibers. Therefore, we should calculate the molecular weight of the whole nanoparticle. For DOTA-Gd, the molecular weight is 580.62 due to the DOTA-Gd could move in solution freely. For nanoparticle (Ppdf-Gd without MMP-2), the molecular weight is 3293.55 × N (the molecular weight of the monomer × the numbers of monomer assembled into nanoparticle). For nanofiber (Ppdf-Gd with MMP-2), the molecular weight is 1794.18 × M (the molecular weight of M2 × the numbers of monomer assembled into nanofiber). Although molecular weight of Ppdf-Gd decreased with treatment of MMP-2, the nanofiber self-assembly was much larger than sphere nanoparticles (TEM in Fig. 2), indicating the value of M should be much larger than that of N. As a result, nanofibers should have a higher molecular weight than nanoparticles and the

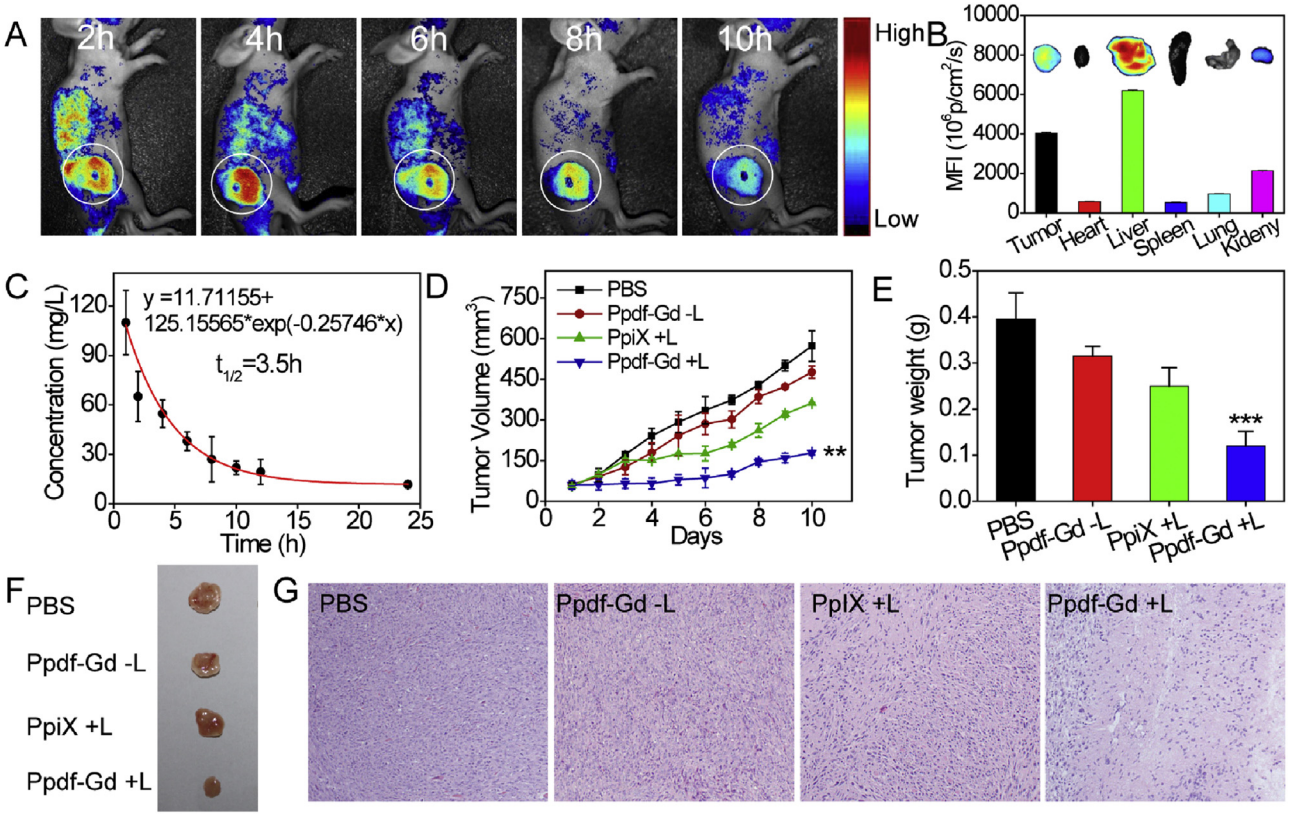

Fig. 5. (A) Fluorescence images of Ppdf-Gd *via i.v.* injection at different time points. The white circles indicated the tumor region. (B) The mean fluorescence intensity of various organs and tumor at 24 h postinjection. (C) Pharmacokinetics of Ppdf-Gd after intravenous injection. (D) Tumor volume changes of SCC-7 bearing mice. (E) Average tumor weight of various groups and (F) photographs of tumor at the ending of treatment. (G) H&E stained histological section of tumor in different groups. Date are means ± s.d. (n = 4), the statistical analysis was determined by Student's t-test (*p < 0.05, **p < 0.01, ***p < 0.001).

molecular weight of DOTA-Gd is the smallest. This difference in molecular weight might cause a relaxivity change. To confirm it, the relaxation time of various samples was measured on 4.7 T MRI scanner. At 25 °C and neutral pH, the r_1 value of Ppdf-Gd (Fig. 4B) was evaluated to be 28.17 $mM^{-1}s^{-1}$, which was significantly higher than that of small molecular contrast agents DOTA-Gd (~4 $mM^{-1}s^{-1}$). The higher r_1 of Ppdf-Gd was due to the fact that the molecular weight of free DOTA-Gd (580.62) was obviously lower than that of Ppdf-Gd even in a monomeric state (3293.55) (Fig. 4A). Moreover, when Ppdf-Gd was incubated with enzyme MMP-2, the r_1 value of Ppdf-Gd was further evaluated to 51.52 $mM^{-1}s^{-1}$, which is nearby 1.8-fold to that of spherical nanoparticles. Meanwhile, the relaxation rate of Pdf-Gd group did not change whether addition of MMP-2 or not (Fig. S8). Under MMP-2 enzyme, spherical nanoparticles can assemble into nanofibers through *β*-sheets within peptide chain and lateral π-π stacking interaction among phenyl rings [32]. The long nanofiber is composed of more monomers in regular arrangement, which has greater molecular weight and longer rotational correlation time compare to spherical counterparts [25,26]. According to the above theory, the relaxivity increment was due to MMP-2 triggered sphere-to-fibers transformation.

To further examine the feasibility of the MMP-2 triggered amplified MRI *in vivo*. The T1-weighted MR image was conducted in the SCC-7 tumor-bearing nude mouse. The MR images of tumor region were obtained at pre-injection, 1 h and 3 h postinjection. As shown in Fig. 4C, compared with preinjection (0 h), DOTA, Ppdf-Gd and Pdf-Gd had a brightening effect in tumor area at 1 h postinjection. Quantitative results (Fig. 4D) revealed that the percentage of signal intensity increment was 18.3%, 18.5% and 21% for DOTA-Gd, Pdf-Gd and Ppdf-Gd, respectively. After 3 h postinjection, the MRI signal of DOTA-Gd slightly decreased (16.4%), partly due to the rapid clearance of DOTA-Gd *in vivo* [5,39]. On the contrary, a continuous signal increment was discovered in Ppdf-Gd (23.4%) and Pdf-Gd (40.3%), suggesting that the Ppdf-Gd or Pdf-Gd could better accumulate in tumor over time. What's more, Ppdf-Gd showed a better imaging performance than Pdf-Gd probably due to increment of relaxivity under enzyme MMP-2.

Some previous reports indicated that the content and retention time of Au and Fe can be improved by the aggregation of gold nanoparticles and Fe_3O_4 nanoparticles in the tumor microenvironment [40–42]. Except for the enhancement of relaxation rate, the concentration difference may also attribute to the enhanced MRI. Quantitative analysis of Gd content in various organs was measured by inductively coupled plasma mass spectrometry (ICP-MS). The main organs and tumor were exfoliated and digested for ICP-MS test at 3 and 24 h postinjection. At 3 h postinjection, the Gd content in Ppdf-Gd group in tumor area was nearby 1.53-fold to that in Pdf-Gd (Fig. 4E). Moreover, this ratio has changed to 2.01 at 24 h postinjection, indicating that Ppdf-Gd can promote the accumulation of Gd in tumor. To further confirm it, an extended time MRI *in vivo* was conducted (Fig. S9A). As shown in Fig. S9B, the quantitative result revealed that Ppdf-Gd reached the maximum accumulation at 5 h postinjection while Pdf-Gd reached reached the maximum accumulation at 4 h (Fig. S9B). Longer accumulation time in Ppdf-Gd group could lead to more Gd accumulation in the tumor. Besides, the imaging effect in Ppdf-Gd was better than that in Pdf-Gd after 3 h postinjection. These results suggested that the sphere-to-fiber transformation could facilitate Ppdf-Gd to accumulate better in tumor. Particles with large size could restrict the peptide self-assembled in tumor and avoid the reenter to blood vessel, leading to improved accumulation in tumor. All these results suggested that the amplified MRI signal of Ppdf-Gd *in vivo* was due to both the increased relaxivity and the enhanced accumulation of Gd^{3+}. This dual-stage-amplified MRI signal *in vivo* should have significant meaning, since it provided a precise and important irradiation window for photodynamic therapy.

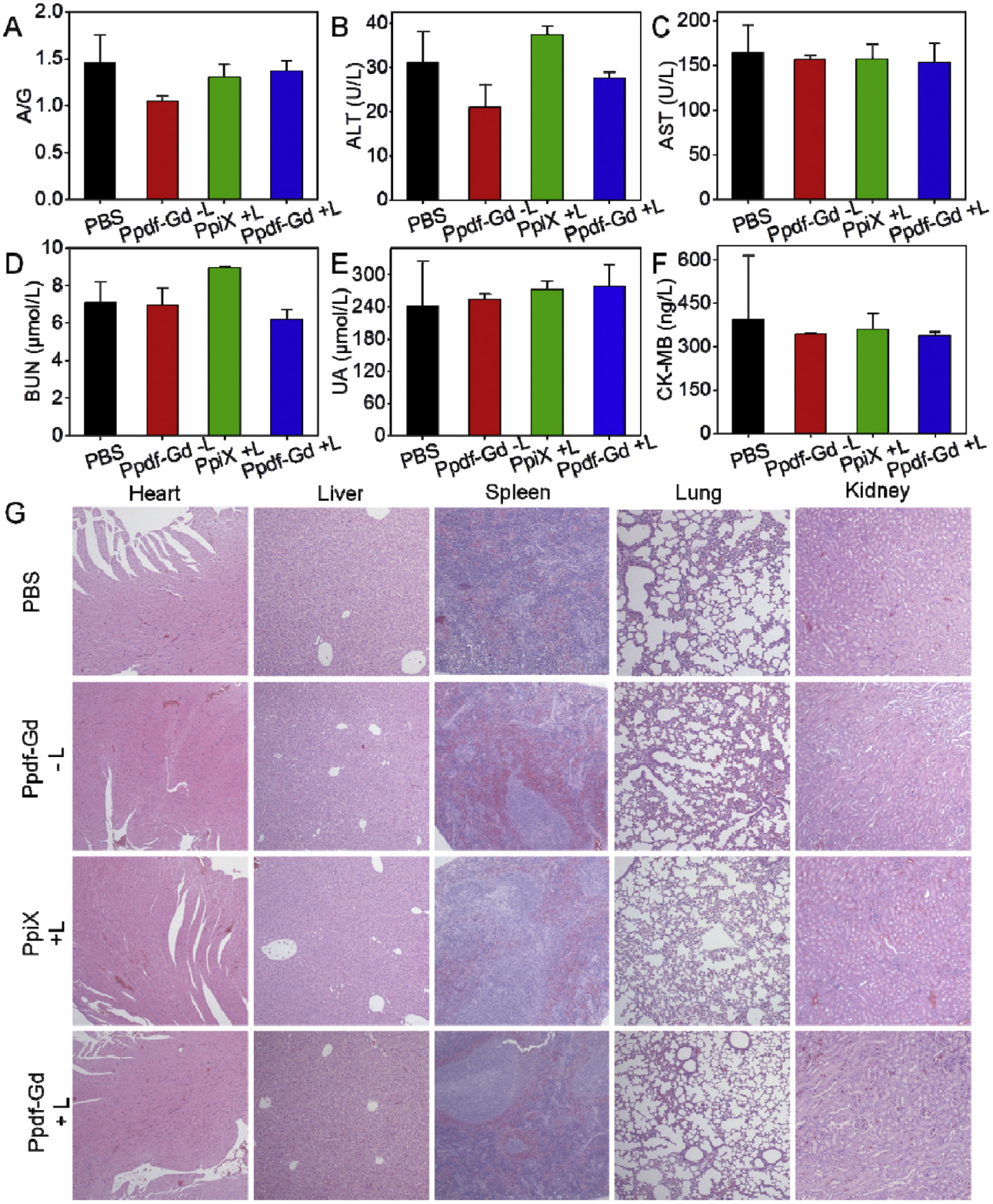

Fig. 6. Blood routine analysis of (A) A/G, (B) ALT, (C) AST, (D) BUN, (E) UA, and (F) CK-MB at the end of treatment. (G) H&E staining of heart, liver, spleen, lung, and kidneys with various samples.

Noted that the Ppdf-Gd had 1.5-fold more accumulation and 1.8-fold higher relaxivity, when compared with the Ppd-Gd. However, the enhancement of MRI *in vivo* was not enough satisfactory due to the following reasons: (i) highly heterogeneous distribution of MMP-2 in tumor resulted in the Ppdf-Gd incomplete cleavage at a short time; (ii) the accumulated concentration of Ppdf-Gd in the tumor site is not as high as *in vitro*; (iii) the Ppdf-Gd could not accomplish sphere-to-fiber transformation immediately due to the reassembly of peptide would take time. These issues motivated us to further refine the nanomaterials base on this MRI enhancement mechanism.

3.5. Tumor targeted imaging and antitumor efficacy in vivo

Considering that the fluorescence of PpiX could also be employed to monitor the *in vivo* biodistribution of Ppdf-Gd, fluorescence imaging *in vivo via* intravenously (*i.v.*) injection was investigated at different time points. As shown in Fig. 5A, obvious fluorescence signal was found in the tumor region and reached a maximum within 4 h, suggesting that Ppdf-Gd could effectively accumulate in tumor tissue. At 24 h post-injection, main organs and tumor were exfoliated and imaged. It was found that MFI in tumor was significantly higher than that in other organs including the metabolic organ kidney (Fig. 5B). Note that there existed a discrepancy between the results of ICP-MS and fluorescence imaging, especially in spleen. Since spleen contained a large amount of redundant red blood cell, which had high absorbance of the PpiX emission, leading in the undetectable fluorescence in spleen [43]. Besides, pharmacokinetics study found that the blood circulation half-life ($t_{1/2}$) of Ppdf-Gd was around 3.5 h (Fig. 5C), which significantly higher than that of DOTA-Gd [44].

The cell toxicity of Ppdf-Gd was measured *via* MTT assay and confocal laser scanning microscope (CLSM). Ppdf-Gd presented negligible cell dark-toxicity, suggesting the well biocompatibility (Fig. S10). However, obvious toxicity was observed when Ppdf-Gd received light irradiation, and the toxicity was concentration-dependent.

For *in vivo* study, the therapeutic efficacy of Ppdf-Gd was assessed using SCC-7 tumor bearing nude mice. The tumor volume and body weight had recorded over the course of treatment. As shown in Fig. 5D, a significant suppression effect was observed in Ppdf-Gd with light irradiation. For comparison, the PBS and Ppdf-Gd without light irradiation hardly inhibited tumor growth, while PpiX group with light irradiation could retard tumor growth so some extent. The tumor was exfoliated at the end of treatment, the tumor weight (Fig. 5E) and photographs (Fig. 5F) showed that tumors in Ppdf-Gd group with light irradiation were significant smaller than other groups, which was in agreement with the result of average tumor volume. Furthermore, hematoxylin-eosin (H&E) staining was carried out to further evaluate therapeutic efficacy. As shown in Fig. 5G, dense tumor cell nuclei (blue dots) in PBS and Ppdf-Gd groups without light irradiation were observed, while massive nuclei absence appeared in Ppdf-Gd with light irradiation, suggesting that Ppdf-Gd can induce most tumor cell death during PDT period.

3.6. Systemic toxicity evaluation

The potential systemic toxicity of Ppdf-Gd was assessed by blood routine analysis. The liver toxicity was assessed by the expression level of liver function markers. Negligible difference was observed among various samples in the expression of albumin/globulin ratio (A/G, Fig. 6A), alanine aminotransferase (ALT, Fig. 6B) and aspartate aminotransferase (AST, Fig. 6C). The indexes of kidney function markers in terms of blood urea nitrogen (BUN, Fig. 6D), uric acid (UA, Fig. 6E) and heart function markers creatine kinase MB isoenzyme (CK-MB, Fig. 6F) were also in the normal range [45,46]. These results indicated that the Ppdf-Gd did not cause any toxicity in liver, kidney and heart, similar results also appeared in the group of Pdf-Gd with light irradiation.

To directly observe the potential side effects, H&E staining of various organs was conducted to observe the morphology. As shown in Fig. 6G, the images of spleen, lung, heart, liver, and kidney of various groups have shown undetectable morphology changes, which were consistence with the blood routine analysis, suggesting that Ppdf-Gd have the low systemic toxicity. The little side effect was due to toxic ROS molecules only generated in light irradiation region, the accurate location of laser light efficiently restricted phototoxicity in tumor region. So dual-stage-amplified MRI can provide precise information about irradiation region, which was meaningful for improving clinical translation of PDT.

4. Conclusions

In summary, we have developed a MMP-2 responsive chimeric peptide to realize dual-stage-amplified MRI-guided precise PDT. The chimeric peptide can self-assembly to spherical nanoparticle in physiological conditions and transform into long nanofibers by reducing the CAC value under enzyme MMP-2. The sphere-to-fibers transformation can increase the local Gd^{3+} concentration in tumor and thus improved MRI signal. Importantly, the transformation of molecular structure can improve the relaxivity of Gd^{3+} chelate by prolonging rotational correlation for further enhanced MRI. This dual-stage-amplified MRI strategy *via* enzyme-triggered transformation in tumor can improve the relaxivity and sensitivity of clinical Gd^{3+} chelates, which should provide great potential for developing supramolecular contrast agent to MRI applications *in vivo*.

Acknowledgements

This work was supported by National Natural Science Foundation of China (21778020 and 51603080), the Fundamental Research Funds for the Central Universities (2662015QD026) and Sci-tech Innovation Foundation of Huazhong Agriculture University (2662017PY042 and 2662018PY024). We thank Wuhan Institute of Physics and Mathematics and Wuhan Institute of Virology, Chinese Academy of Sciences, for our MR imaging and *in vivo* fluorescence imaging work.

Appendix A. Supplementary data

Supplementary data related to this article can be found at https://doi.org/10.1016/j.biomaterials.2018.08.026.

References

[1] A. Accardo, D. Tesauroa, L. Aloj, C. Pedone, G. Morelli, Supramolecular aggregates containing lipophilic Gd (III) complexes as contrast agents in MRI, Coord. Chem. Rev. 253 (2009) 2193–2213.
[2] R. Bardhan, S. Lal, A. Joshi, N.J. Halas, Theranostic nanoshells: from probe design to imaging and treatment of cancer, Acc. Chem. Res. 44 (2011) 936–946.
[3] E.K. Lim, T. Kim, S. Paik, S. Haam, Y.M. Huh, K. Lee, Nanomaterials for theranostics: recent advances and future challenges, Chem. Rev. 115 (2015) 327–394.
[4] M.C. Heffern, L.M. Matosziuk, T.J. Meade, Lanthanide probes for bioresponsive imaging, Chem. Rev. 114 (2014) 4496–4539.
[5] A.J.L. Villaraza, A. Bumb, M.W. Brechbiel, Macromolecules, dendrimers, and nanomaterials in magnetic resonance imaging: the interplay between size, function, and pharmacokinetics, Chem. Rev. 110 (2010) 2921–2959.
[6] Y. Song, X. Xu, K.W. MacRenaris, X.Q. Zhang, C.A. Mirkin, T.J. Meade, Multimodal gadolinium-enriched DNA-gold nanoparticle conjugates for cellular imaging, Angew. Chem. Int. Ed. 48 (2009) 9143–9147.
[7] T. Courant, V.G. Roullin, C. Cadiou, M. Callewaert, M.C. Andry, C. Portefaix, C. Hoeffel, M.C. de Goltstein, M. Port, S. Laurent, L.V. Elst, R. Muller, M. Molinari, F. Chuburu, Hydrogels incorporating GdDOTA: towards highly efficient dual T_1/T_2 MRI contrast agents, Angew. Chem. Int. Ed. 51 (2012) 9119–9122.
[8] D. Ni, J. Zhang, J. Wang, P. Hu, Y. Jin, Z. Tang, Z. Yao, W. Bu, J. Shi, Oxygen vacancy enables markedly enhanced magnetic resonance imaging-guided photothermal therapy of a Gd^{3+}-doped contrast agent, ACS Nano 11 (2017) 4256–4264.
[9] M.H. Lee, E.J. Kim, H. Lee, H.M. Kim, M.J. Chang, S.Y. Park, K.S. Hong, J.S. Kim, J.L. Sessler, Liposomal texaphyrin theranostics for metastatic liver cancer, J. Am. Chem. Soc. 138 (2016) 16380–16387.
[10] H. Yuan, C. Xu, Y. Zhao, B. Yu, G. Cheng, F.J. Xu, Well-defined protein-based supramolecular nanoparticles with excellent MRI abilities for multifunctional delivery systems, Adv. Funct. Mater. 26 (2016) 2855–2865.
[11] Z. Zhou, M. Qutaish, Z. Han, R.M. Schur, Y. Liu, D.L. Wilson, Z.R. Lu, MRI detection of breast cancer micrometastases with a fibronectin-targeting contrast agent, Nat. Commun. 6 (2015) 7984–7995.
[12] E.S. Olson, T. Jiang, T.A. Aguilera, Q.T. Nguyen, L.G. Ellies, M. Scadeng, R.Y. Tsien, Activatable cell penetrating peptides linked to nanoparticles as dual probes for in vivo gluorescence and MR imaging of proteases, Proc. Natl. Acad. Sci. U.S.A. 107 (2010) 4311–4316.
[13] H. Zhou, W. Qian, F.M. Uckun, L. Wang, Y.A. Wang, H. Chen, Q. Yu Kooby, M. Lipowska, C.A. Staley, H. Mao, L. Yang, IGF1 receptor targeted theranostic nanoparticles for targeted and image-guided therapy of pancreatic cancer, ACS Nano 9 (2015) 7976–7991.
[14] M. Lepage, W.C. Dow, M. Melchior, Y. You, B. Fingleton, C.C. Quarles, C. Pepin, J.C. Gore, L.M. Matrisian, J.O. McIntyre, Noninvasive detection of matrix metalloproteinase activity in vivo using a novel magnetic resonance imaging contrast

agent with a solubility switch, Mol. Imag. 6 (2007) 393–403.
[15] X.L. Hu, G.H. Liu, Y. Li, X.R. Wang, S.Y. Liu, Cell-penetrating hyperbranched polyprodrug amphiphiles for synergistic reductive milieu-triggered drug release and enhanced magnetic resonance signals, J. Am. Chem. Soc. 137 (2015) 362–368.
[16] Z. Zhao, H. Fan, G. Zhou, H. Bai, H. Liang, X. Zhang, W. Tan, Activatable fluorescence/MRI bimodal platform for tumor cell imaging via MnO_2 nanosheet-aptamer nanoprobe, J. Am. Chem. Soc. 136 (2014) 11220–11223.
[17] M.L. Viger, J. Sankaranarayanan, C. de Gracia Lux, M. Chan, A. Almutairi, Collective activation of MRI agents via encapsulation and disease-triggered release, J. Am. Chem. Soc. 135 (2013) 7847–7850.
[18] T.T. Wang, D.G. Wang, H.J. Yu, M.W. Wang, J.P. Liu, B. Feng, F.Y. Zhou, Q. Yin, Z.W. Zhang, Y.Z. Huang, Y.P. Li, Intracellularly acid-switchable multifunctional micelles for combinational photo/chemotherapy of the drug-resistant tumor, ACS Nano 10 (2016) 3496–3508.
[19] D.L. Ni, Z.W. Shen, J.W. Zhang, C. Zhang, R.H. Wu, J.N. Liu, M.Z. Yi, J. Wang, Z.W. Yao, W.B. Bu, J.L. Shi, Integrating anatomic and functional dual-mode magnetic resonance imaging: design and applicability of a bifunctional contrast agent, ACS Nano 10 (2016) 3783–3790.
[20] R.X. Song, M. Zhang, Y.Y. Liu, Z.W. Cui, H. Zhang, Z.M. Tang, X.Y. Chen, H.H. Wu, Z.W. Yao, M.Y. He, W.B. Bu, A multifunctional nanotheranostic for the intelligent MRI diagnosis and synergistic treatment of hypoxic tumor, Biomaterials 175 (2018) 123–133.
[21] L.M. Randolph, C.L.M. LeGuyader, M.E. Hahn, C.M. Andolina, J.P. Patterson, R.F. Mattrey, J.E. Millstone, M. Botta, M. Scadeng, N.C. Gianneschi, Polymeric Gd-DOTA amphiphiles form spherical and fibril-shaped nanoparticle MRI contrast agents, Chem. Sci. 7 (2016) 4230–4236.
[22] A. Ghosh, M. Haverick, K. Stump, X. Yang, M.F. Tweedle, J.E. Goldberger, Fine-tuning the pH trigger of self-assembly, J. Am. Chem. Soc. 134 (2012) 3647–3650.
[23] D. Zhang, G. Qi, Y. Zhao, S. Qiao, C. Yang, H. Wang, In situ formation of nanofibers from purpurin18－peptide conjugates and the assembly induced retention effect in tumor sites, Adv. Mater. 27 (2015) 6125–6130.
[24] I. Kim, E.H. Han, J. Ryu, J.Y. Min, H. Ahn, Y.H. Chung, E. Lee, One-dimensional supramolecular nanoplatforms for theranostics based on co-assembly of peptide amphiphiles, Biomacromolecules 17 (2016) 3234–3243.
[25] C. Diaferia, E. Gianolio, P. Palladino, F. Arena, C. Boffa, G. Morelli, A. Accardo, Peptide materials obtained by aggregation of polyphenylalanine conjugates as gadolinium-based magnetic resonance imaging contrast agents, Adv. Funct. Mater. 25 (2015) 7003–7016.
[26] A.T. Preslar, G. Parigi, M.T. McClendon, S.S. Sefick, T.J. Moyer, C.R. Haney, E.A. Waters, K.W. MacRenaris, C. Luchinat, S.I. Stupp, Gd(III)-labeled peptide nanofibers for reporting on biomaterial localization in vivo, ACS Nano 8 (2014) 7325–7332.
[27] S.R. Bull, M.O. Guler, R.E. Bras, T.J. Meade, S.I. Stupp, Ratiometric biosensor for aggregation-induced emission-guided precise photodynamic therapy, ACS Nano 9 (2015) 10268–10277.
[28] H. Maeda, J. Wu, T. Sawa, Y. Matsumura, K. Hori, Tumor vascular permeability and the EPR effect in macromolecular therapeutics: a review, J. Contr. Release 65 (2000) 271–284.
[29] W.H. Chen, G.F. Luo, W.X. Qiu, Q. Lei, L.H. Liu, D.W. Zheng, S. Hong, S.X. Cheng, X.Z. Zhang, Tumor-triggered drug release with tumor-targeted accumulation and elevated drug retention to overcome multidrug resistance, Chem. Mater. 28 (2016) 6742–6752.
[30] M.M. Nguyen, A.S. Carlini, M.P. Chien, S. Sonnenberg, C. Luo, R.L. Braden, K.G. Osborn, Y. Li, N.C. Gianneschi, K.L. Christman, Enzyme-responsive nanoparticles for targeted accumulation and prolonged retention in heart tissue after myocardial infarction, Adv. Mater. 27 (2015) 5547–5552.
[31] N. Tzokova, C.M. Fernyhough, M.F. Butler, S.P. Armes, A.J. Ryan, P.D. Topham, D.J. Adams, The effect of PEO length on the self-assembly of poly (ethylene oxide)－tetrapeptide conjugates prepared by “click” chemistry, Langmuir 25 (2009) 11082–11089.
[32] N. Tzokova, C.M. Fernyhough, P.D. Topham, N. Sandon, D.J. Adams, M.F. Butler, S.P. Armes, A.J. Ryan, Soft hydrogels from nanotubes of poly (ethylene oxide)-tetraphenylalanine conjugates prepared by click chemistry, Langmuir 25 (2009) 2479–2485.
[33] V. Castelletto, I.W. Hamley, Self-assembly of a model amphiphilic phenylalanine peptide/polyethylene glycol block copolymer in aqueous solution, Biophys. Chem. 141 (2009) 169–174.
[34] C. Diaferia, F.A. Mercurio, C. Giannini, T. Sibillano, G. Morelli, M. Leone, A. Accardo, Self-assembly of PEGylated tetra-phenylalanine derivatives: structural insights from solution and solid state studies, Sci. Rep. 6 (2016) 26638–26650.
[35] M.T. Jeena, L. Palanikumar, E.M. Go, I. Kim, M.G. Kang, S. Lee, S. Park, H. Choi, C. Kim, S.M. Jin, S.C. Bae, H.W. Rhee, E. Lee, S.K. Kwak, J.H. Ryu, Mitochondria localization induced self-assembly of peptide amphiphiles for cellular dysfunction, Nat. Commun. 8 (2017) 26–36.
[36] R.B. Lauffer, Paramagnetic metal complexes as water proton relaxation agents for NMR imaging: theory and design, Chem. Rev. 87 (1987) 901–927.
[37] P. Caravan, J.J. Ellison, T.J. McMurry, R.B. Lauffer, Gadolinium(III) chelates as MRI contrast agents: structure, dynamics, and applications, Chem. Rev. 99 (1999) 2293–2352.
[38] P. Verwilst, S. Park, B. Yoon, J.S. Kim, Recent advances in Gd-chelate based bimodal optical/MRI contrast agents, Chem. Soc. Rev. 44 (2015) 1791–1806.
[39] E. Wiener, M.W. Brechbiel, H. Brothers, R.L. Magin, O.A. Gansow, D.A. Tomalia, P.C. Lauterbur, Dendrimer-based metal chelates: a new class of magnetic resonance imaging contrast agents, Magn. Reson. Med. 31 (1994) 1–8.
[40] S. Ruan, C. Hu, X. Tang, X. Cun, W. Xiao, K. Shi, Q. He, H. Gao, Increased gold nanoparticle retention in brain tumors by in situ enzyme-induced aggregation, ACS Nano 10 (2016) 10086–10098.
[41] Z. Gao, Y. Hou, J. Zeng, L. Chen, C. Liu, W. Yang, M. Gao, Tumor microenvironment-triggered aggregation of anti-phagocytosis ^{99m}Tc-labeled Fe_3O_4 nanoprobes for enhanced tumor imaging in vivo, Adv. Mater. 29 (2017) 1701095–1701102.
[42] S. Wang, P. Huang, X. Chen, Hierarchical targeting strategy for enhanced tumor tissue accumulation/retention and cellular internalization, Adv. Mater. 28 (2016) 7340–7364.
[43] Matti M. van Schooneveld, E. Vucic, R. Koole, Y. Zhou, J. Stocks, D.P. Cormode, C.Y. Tang, R.E. Gordon, K. Nicolay, A. Meijerink, Z.A. Fayad, W.J.M. Mulder, Improved biocompatibility and pharmacokinetics of silica nanoparticles by means of a lipid coating: a multimodality investigation, Nano Lett. 8 (2008) 2517–2525.
[44] J.C. Bousquet, S. Saini, D.D. Stark, P.F. Hahn, M.A.D.H.U. Nigam, J. Wittenberg, J.T. Ferrucci Jr., Gd-DOTA: characterization of a new paramagnetic complex, Radiology 166 (1988) 693–698.
[45] Z. Zhao, X. Wang, Z. Zhang, H. Zhang, H. Liu, X. Zhu, H. Li, X. Chi, Z. Yin, J. Gao, Real-time monitoring of arsenic trioxide release and delivery by activatable T1 imaging, ACS Nano 9 (2015) 2749–2759.
[46] K. Han, W.Y. Zhang, J. Zhang, Q. Lei, S.B. Wang, J.W. Liu, X.Z. Zhang, H.Y. Han, Acidity-triggered tumor-targeted chimeric peptide for enhanced intra-nuclear photodynamic therapy, Adv. Funct. Mater. 26 (2016) 4351–4361.